

This is an electronic reprint of the original article. This reprint may differ from the original in pagination and typographic detail.

---

## Electro-Optical Coupling in Double Diode Structures

Anttu, Nicklas; Dagytė, Vilgailė; Behaghel, Benoît; Radevici, Ivan; Sadi, Toufik; Kivisaari, Pyry; Oksanen, Jani

*Published in:*  
Physical Review Applied

*DOI:*  
<https://doi.org/10.1103/PhysRevApplied.19.064054>

Published: 01/01/2023

*Document Version*  
Final published version

*Document License*  
Publisher rights policy

[Link to publication](#)

*Please cite the original version:*

Anttu, N., Dagytė, V., Behaghel, B., Radevici, I., Sadi, T., Kivisaari, P., & Oksanen, J. (2023). Electro-Optical Coupling in Double Diode Structures. *Physical Review Applied*, 19, Article 064054.  
<https://doi.org/10.1103/PhysRevApplied.19.064054>

### General rights

Copyright and moral rights for the publications made accessible in the public portal are retained by the authors and/or other copyright owners and it is a condition of accessing publications that users recognise and abide by the legal requirements associated with these rights.

### Take down policy


If you believe that this document breaches copyright please contact us providing details, and we will remove access to the work immediately and investigate your claim.

## Electro-Optical Coupling in Double Diode Structures

Nicklas Anttu<sup>1,\*</sup>, Vilgailė Dagytė<sup>2,†</sup>, Benoît Behaghel<sup>2</sup>, Ivan Radevici<sup>2</sup>, Toufik Sadi<sup>2</sup>,  
Pyrö Kivisaari<sup>2</sup> and Jani Oksanen<sup>2</sup>

<sup>1</sup>*Physics, Faculty of Science and Engineering, Åbo Akademi University, FI-20500 Turku, Finland*

<sup>2</sup>*Engineered Nanosystems Group, Aalto University, Aalto 00076, Finland*

 (Received 10 March 2023; revised 12 May 2023; accepted 23 May 2023; published 16 June 2023)

Alternative types of artificial cooling techniques are of large interest for multiple applications. Here, we develop a framework for studying the role of electro-optical coupling in the analysis of solid-state refrigerators based on electroluminescent cooling (ELC) by combining device measurements with optical simulations. The studied device consists of a light-emitting diode (LED) epitaxially connected to a photodetector (PD) in a double-diode structure (DDS). Previous results of the DDS have indicated that the LED side already operates at conditions corresponding to ELC, but Ohmic losses and imperfect photodetection of the LED light in the PD have prevented observing the effect directly. Here, to break down the detection losses of the DDS, we report on the electro-optical response of the LED and the PD in detail, as well as the role of the spectral coupling from the LED to the PD. We present a detailed framework for combining measurements and simulations of the DDS to gain quantitative insight of the electro-optical response of the LED and PD, as well as the coupling between them, including the analysis of effects that are not directly accessible by standard measurements. The developed approach allows identifying the different photodetection loss mechanisms from the current-voltage and electroluminescence measurements and thereby gives guidance for designs toward a direct demonstration of ELC at practically relevant cooling powers. Somewhat surprisingly, the results show that an imperfect spectral absorption efficiency of the PD, in addition to its below unity quantum efficiency, are together required to explain the previously observed low photodetection efficiency of the DDS even for several microns thick PD structures. In comparison, the LED top mirror introduces only a minuscule drop in photodetection efficiency. Put in plain numbers, our analysis reveals that in the current DDS designs, there is headroom by 14% in the spectral matching between the LED and the PD, 5% in the charge collection efficiency of the PD, and 4% in the efficiency at which photons emitted from the LED reach the PD.

DOI: [10.1103/PhysRevApplied.19.064054](https://doi.org/10.1103/PhysRevApplied.19.064054)

### I. INTRODUCTION

Light-emitting diodes (LEDs) have revolutionized general lighting during the last decade, and overall, they represent one of the core enabling technologies behind the rapidly growing field of photonics [1–3]. However, not only are LEDs efficient light emitters, but they can be more broadly seen as thermodynamic engines capable of near-reversible conversion between electrical, thermal, and optical energy [4]. Accordingly, an LED generally feeds on both electrical and thermal energy while emitting light, giving rise to the possibility of electroluminescent cooling (ELC). The physics behind ELC has been postulated already decades ago [5–8], but demonstrations of it at a practical level are still in the making.

The basic principle of ELC starts from boosting the thermal radiation of a semiconductor through an externally applied bias voltage, giving rise to a nonzero photon chemical potential in the semiconductor [9]. This allows amplifying the thermal band-to-band light emission exponentially. Meanwhile, using a bias voltage smaller than the band-gap energy ensures that the average electrical energy of the injected electron-hole pairs is lower than the average energy of the emitted photons. In practice, this means that between injection and recombination events, the electron-hole pairs gain extra energy by thermalizing to the lattice temperature through phonon absorption. Once the external quantum efficiency (EQE) of light emission is high, most of the recombination events end up generating photons that remove heat out of the device. ELC shares most of its basic physics with laser cooling [10–12], but perhaps the largest practical difference is that in ELC, the average energy of the input quanta ( $e$ - $h$  pairs) may be considerably lower than the band-gap energy. This allows much

\*nicklas.anttu@abo.fi

†These authors contributed equally.

more leeway in the required EQE of the emission as compared to laser cooling. ELC can also be regarded as a subfield of the much broader research area concerning the thermodynamics of light in solids and related applications [13–22], where thermophotovoltaics is perhaps the most well-known topic [18–22].

It is clear that a practical demonstration of ELC would have inherent scientific value, as it would showcase a fundamental physical effect postulated already decades ago. But perhaps even more importantly, such a successful demonstration would also naturally present the question of whether ELC could have added value on top of other cooling technologies available today. Shortly comparing its potential with only the two most dominant ones, ELC could first of all outperform thermoelectric coolers in efficiency [23], as well as extend the attainable temperatures towards the high- $T$  superconductor regime [4]. Even as compared to the ubiquitous mechanical heat pumps, ELC could match their efficiency and additionally enable getting rid of all the moving parts.

To date, ELC has been indirectly observed only at extremely small cooling powers [24]. The concept has also been demonstrated to thermally enhance the efficiency of visible LEDs [25], and the closely related phenomenon of negative luminescence cooling has also been directly observed in near-field coupled nanocalorimetric experiments [17]. Therefore, one can say that the field is now calling for an irrefutable demonstration of cooling at typical LED operating regimes on the order of  $\text{W}/\text{cm}^2$  in cooling power density in mm-scale devices. To this end, our previous work has introduced a prototype structure known as a double-diode structure (DDS), integrating an LED and a photodetector (PD) as a single semiconductor device. In the DDS, we (1) inject electrical current to the LED to generate light and (2) detect absorption of the generated photons as photocurrent in the PD. These studies indicate that optical cooling takes place already locally inside the device, once the effect of losses taking place outside the active region of the LED is accounted for [26]. Thus, it appears that what prevents the actual cooling from being directly observed is a combination of different factors, including inner and outer electrical resistances, current crowding, and optical losses. The contribution of all of these factors should be quantified separately to lead the way towards direct demonstration of ELC, e.g., by developing optically invisible thermal insulators in the form of vacuum nanogaps between the emitter and absorber elements of the DDS [4].

In this paper, we study and analyze in detail the electro-optical coupling taking place between the LED and the PD in the DDS to lay ground for more direct demonstration and technical applications of the ELC effect. Our study reveals which processes limit the performance and enables a design approach for future improvements for the DDS. We present a detailed framework for combining

measurements and simulations of the DDS to gain quantitative understanding of the electro-optical response of the LED and PD, as well as the coupling between them, including the analysis of effects that are not directly accessible by standard measurements. In a broader sense, our framework should be straightforward to adapt also for the analysis of the coupling and losses in other closely related, emerging photonic power conversion devices, such as laser power converters [27,28].

In our analysis approach, the photodetection efficiency in the DDS is split into three multiplicative efficiencies as  $\xi = \eta_{\text{optical}} \eta_{\text{matching}} \eta_{\text{CCE}}$ . Here,  $\eta_{\text{optical}}$  is the efficiency at which the photons generated by the LED are transported to the PD,  $\eta_{\text{matching}}$  represents the spectral matching (efficiency) between the PD and LED to absorb the transported light and convert it into electron-hole pairs, and  $\eta_{\text{CCE}}$  is the charge collection efficiency of the PD, that is, the efficiency at which the PD collects the photogenerated electron-hole pairs to generate the photocurrent. To extract these three factors, we use a combination of electrical and optical measurements and simulations.

The paper is organized as follows. In Sec. II A, we introduce the three DDSs that we study, in Sec. II B we present the measurements and simulation methods used for analyzing the electro-optical coupling in the DDS, in Sec. III we show the results from the analysis, in Sec. IV we discuss the implication of our results on achieving ELC, and in Sec. V we conclude and summarize the main findings of our study.

## II. METHODS

### A. DDS samples

Three DDSs based on 1-mm-diameter circular mesas are studied (Fig. 1 and Table I). The main difference between the three DDSs is the type of PD, as well as the presence (HJ-1), or lack thereof (HJ-2, DHJ-1), of an omnidirectional reflector (ODR) on the top side of the LED. The devices have three separate 20-nm-thick GaAs contact layers—one top contact above the LED, one middle contact between the LED and the PD, and one bottom contact under the PD. These three contacts allow separate electrical access to the LED and PD in the electrical characterization of the DDS [see Fig. 1(a) for a schematic of electrical contacting]. A listing of all the device layers is given in Ref. [29].

All three DDSs have a similar LED region with a nominally undoped 300-nm-thick GaAs active region surrounded by larger band-gap (Ga, In)P barriers, in a double heterojunction (DHJ) configuration. Two of the samples, called HJ-1 and HJ-2, have a homojunction,  $n$ - $p$  type GaAs PD, with HJ-1 grown by molecular beam epitaxy (MBE), similarly as in Ref. [26], and HJ-2 with metalorganic vapor-phase epitaxy (MOVPE). The third sample, called DHJ-1, is MOVPE grown and has a DHJ GaAs PD.

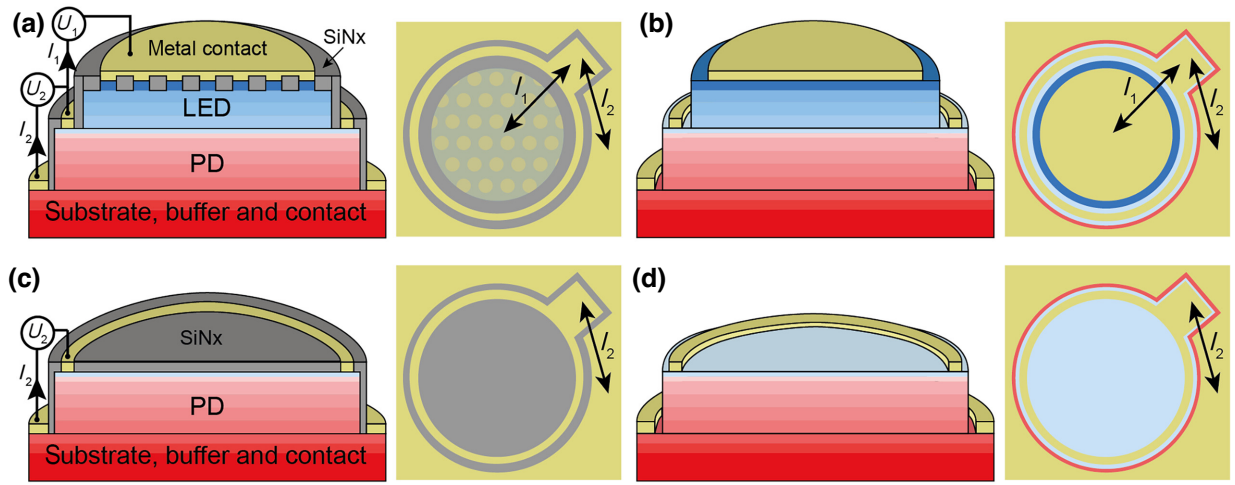


FIG. 1. (a) Cross section and top view of the DDS with a 360-nm  $\text{SiN}_x$  ODR layer (sample HJ-1); (b) the DDS without  $\text{SiN}_x$  (samples HJ-2 and DHJ-1). The corresponding PD-only devices obtained during the same processing procedure are illustrated in (c) for HJ-1 with 360 nm homogeneous  $\text{SiN}_x$  coating and in (d) for HJ-2 and DHJ-1.

The growth details for the MOVPE samples are given in Ref. [30].

HJ-2 and DHJ-1 have a continuous GaAs top contact. In contrast, 93% of the HJ-1 surface is covered by a 360-nm-thick  $\text{SiN}_x$  ODR with the remaining 7% covered by the GaAs top contact. All three DDS structures have a AuZn contacting layer furthest on the top side of the LED.

In order to study the optical response of the PD separately, a dedicated mask design is used during the processing to define, through etching of the LED layers, PD-only mesas next to the full DDS mesas. For HJ-1, the PD is, similarly as the ODR in the full DDS, coated with a  $\text{SiN}_x$  layer [see Fig. 1(c) for the schematic of the PD-only device with the ODR and Fig. 1(d) for the PD-only device without the ODR].

## B. Characterization of DDS response

In the analysis, we use a combination of measurements and optics simulations as summarized in Table IV in Appendix A. With this framework, the electrical response of the system is extracted from measurements. For the optics simulations, we need as input the refractive index and thickness of the constituent layers. This is in contrast

to full electro-optical simulations [31,32], where we need several additional input and fitting parameters related to the electrical properties of each constituent layer [such as doping concentration, electron and hole mobility, recombination parameters (for example interface, non-radiative, Auger and radiative recombination), band gap, and band alignment at interfaces].

### 1. Electrical characteristics: $I$ - $V$ , CQE, LED IQE, and PCE

The electrical characteristics of the DDS are measured using a three-probe arrangement, illustrated in Fig. 1(a), with a Keithley SMU to apply a bias  $U_1$  to the LED and keeping the PD in short-circuit condition ( $U_2 = 0$ ). When the injection current is above 10  $\mu\text{A}$ , the measurements are performed at a low duty cycle with injection pulses not longer than 5.5 ms spaced 2 s apart to limit the risk of possible Ohmic heating degradation of the DDS due to series resistances at high current injection level. Thus, we measure the current  $I_1$  injected into the LED, which gives rise to emission of light and the related current  $I_2$  photogenerated in the PD after absorption of (a fraction of) those photons. The coupling quantum efficiency, directly measurable as  $\eta_{\text{CQE}} = I_2/I_1$ , defines the efficiency of the double diode structure in converting the LED current  $I_1$  to the photogenerated current  $I_2$  in the PD [26]. The internal quantum efficiency (IQE) of the LED,  $\eta_{\text{LED}}$  is the probability that an electrically injected electron-hole pair gives rise to an emitted photon [26]. In the framework of the DDS, it can therefore be expressed as  $\eta_{\text{LED}} = \eta_{\text{CQE}}/\xi$ . The power conversion efficiency for the ELC is defined as  $\eta_{\text{PCE}} = \eta_{\text{LED}} \times (E_{\text{ph}}/qU)$  with  $U$  being the internal bias voltage of the LED (typically,  $U < U_1$  due to external resistances as well as internal spreading resistances) [26],

TABLE I. Summary of the main differences between the three DDSs used in this study.

Sample	PD type	$\text{SiN}_x$ ODR on top of LED	Fabrication method
HJ-1	Homojunction	Yes	MBE
HJ-2	Homojunction	No	MOVPE
DHJ-1	Double hetero- junction	No	MOVPE

$q$  the elementary charge, and  $E_{\text{ph}} \approx 1.42$  eV the energy of the photons emitted by the LED at the band gap of GaAs [33] (at room temperature in our experiments).  $\eta_{\text{PCE}}$  defines the efficiency of transferring energy through radiation from the LED [26].  $\eta_{\text{PCE}} > 1$  thus denotes the criterion for reaching ELC, that is, the LED cooling regime.

## 2. Electroluminescence (EL) of the LED

The (external) EL spectrum  $\Phi_{\text{EL}}(\lambda)$  of the LED as a function of the photon wavelength  $\lambda$  is measured in the same setup as used for the  $I$ - $V$  characterization, with two probes, biasing the LED with a constant 1 mA current and measuring the spectrum of the light emitted through the side of the LED mesa with a fiber spectrometer (Ocean Optics FLAME-S-XR1-ES). This value of 1 mA for the current gives a good signal-to-noise ratio, without exhibiting heating effects in the spectral shape, which show up at higher constant LED current level. We acknowledge that the EL spectra measured through the LED side could, in principle, differ from the spectrum internally emitted by the LED due to wavelength-dependent parasitic absorption before outcoupling at the side of the mesa. However, we find good agreement between measured and modeled EL spectra, indicating that the measurement of the EL through the side of the sample does not strongly distort the spectral shape of the EL (see Fig. S2 within the Supplemental Material [34]).

## 3. EQE of PD-only devices

To elucidate how well the PD performs,  $\eta_{\text{PD}}^{\text{EQE}}(\lambda)$ , the external quantum efficiency (EQE) of the PD-only devices, is measured at normal incidence in an industrial EQE setup (Solar Cell Spectral Response/QE/IPCE Measurement System Model QEX7 from PV Measurements, Inc. — referred to as QEX7 below); see Ref. [35] for additional technical details of the EQE measurements.  $\eta_{\text{PD}}^{\text{EQE}}(\lambda)$  is the fraction of incident photons at wavelength  $\lambda$  converted to photocurrent by the PD. An angle-dependent assessment of the PD EQE would, in principle, be of interest since in the actual DDS, the LED populates all internal propagation angles. However, such EQE measurements are not

straightforward since with external illumination at a planar interface between air and GaAs, we have access only to internal angles less than  $20^\circ$  from normal incidence due to the high refractive index of GaAs.

## 4. Reflectance

We measure the reflectance  $R(\lambda)$  of the PD-only devices to eliminate in our analysis the external reflection loss, which does not exist between the LED and the PD in the DDS layout. Reflectance of the PD-only devices is measured with a FilmTek 200 M setup with a  $5\times$  objective ( $\text{NA} = 0.15$ , corresponding to  $9^\circ$  half-cone angle) and an approximately equal to  $50\ \mu\text{m}$  spot size. Since the FilmTek setup collects light only within this cone of approximately equal to  $9^\circ$  from normal, possible presence of diffuse scattering and reflectance is investigated with total reflectance measurements in an integrating sphere [36], focusing onto the sample with a supercontinuum light source, with a maximum wavelength of 845 nm as limited by its tunable filter (see Sec. S5 within the Supplemental Material [37] for details).

## 5. Coupling from LED to PD

To study in detail the coupling from the LED to the PD in the DDS, we express the CQE as  $\eta_{\text{CQE}} = \xi \times \eta_{\text{LED}}$ . As in our previous study, we express the photodetection efficiency as  $\xi = I_2/I_{\text{rad}}$  with  $I_{\text{rad}}$  being the radiative recombination current of the LED [26]. Of note,  $\xi$  cannot be obtained directly from a measurement of CQE since also  $\eta_{\text{LED}}$  is unknown, and therefore, previously, we used an  $ABC$ -type recombination model to extract  $I_{\text{rad}}$ . As discussed in the introduction, to gain further understanding of the limiting factors of  $\xi$ , here we introduce an analysis of  $\xi$  through three multiplicative factors as  $\xi = \eta_{\text{optical}} \eta_{\text{matching}} \eta_{\text{CCE}}$ , as detailed below (see also Table IV in Appendix A for a summary of the quantities involved in the analysis).

We write  $\xi$  in terms of a wavelength and propagation angle integration of the coupling between the LED and the PD:

$$\begin{aligned} \xi &= \frac{\sum_{\text{TE-TM}} \int \chi_{\text{PD}}(\lambda, \theta) \chi_{\text{optical}}(\lambda, \theta) \Phi_{\text{LED}}(\lambda, \theta) d\lambda d\theta}{\sum_{\text{TE-TM}} \int \Phi_{\text{LED}}(\lambda, \theta) d\lambda d\theta} \\ &= \frac{\sum_{\text{TE-TM}} \int \Phi_{\text{LED-on-PD}}(\lambda, \theta) d\lambda d\theta}{\sum_{\text{TE-TM}} \int \Phi_{\text{LED}}(\lambda, \theta) d\lambda d\theta} \frac{\sum_{\text{TE-TM}} \int \chi_{\text{PD}}(\lambda, \theta) \Phi_{\text{LED-on-PD}}(\lambda, \theta) d\lambda d\theta}{\eta_{\text{CCE}} \sum_{\text{TE-TM}} \int \Phi_{\text{LED-on-PD}}(\lambda, \theta) d\lambda d\theta} \eta_{\text{CCE}} = \eta_{\text{optical}} \eta_{\text{matching}} \eta_{\text{CCE}}. \end{aligned} \quad (1)$$

Here,  $\theta$  is the propagation angle (in the (Ga, In)P layers surrounding the active region of the LED),  $\Phi_{\text{LED}}(\lambda, \theta)$  is the internal EL spectrum of the LED in the DDS in terms

of number of photons/( $\text{m}^2 \text{ s nm}$ ),  $\chi_{\text{optical}}(\lambda, \theta)$  is the optical coupling from the LED to the PD,  $\chi_{\text{PD}}(\lambda, \theta)$  is the IQE of the PD in the DDS, that is, the efficiency for the PD



in the DDS to give rise to a charge carrier in the PD current from an incident photon entering the active region of the PD, and  $\eta_{\text{CCE}}$  is the charge-collection efficiency (CCE) of the PD, that is, the probability that a photogenerated electron-hole pair in the PD gives rise to a charge carrier in the external current.  $\Phi_{\text{LED}}$ ,  $\chi_{\text{optical}}$ , and  $\chi_{\text{PD}}$  show dependence of the polarization state of light, chosen as TE and TM polarization here [38], and in Eq. (1), we perform summing of both polarization states. With this notation  $\Phi_{\text{LED-on-PD}}(\lambda, \theta) = \chi_{\text{optical}}(\lambda, \theta)\Phi_{\text{LED}}(\lambda, \theta)$  in Eq. (1) is then the spectrum incident on the PD (which is also TE-TM dependent).

In Eq. (1),

$$\eta_{\text{optical}} = \frac{\sum_{\text{TE-TM}} \int \Phi_{\text{LED-on-PD}}(\lambda, \theta) d\lambda d\theta}{\sum_{\text{TE-TM}} \int \Phi_{\text{LED}}(\lambda, \theta) d\lambda d\theta} \quad (2)$$

is the efficiency at which photons emitted from the LED reach the active region of the PD, and

$$\eta_{\text{matching}} = \frac{\sum_{\text{TE-TM}} \int \chi_{\text{PD}}(\lambda, \theta) \Phi_{\text{LED-on-PD}}(\lambda, \theta) d\lambda d\theta}{\eta_{\text{CCE}} \sum_{\text{TE-TM}} \int \Phi_{\text{LED-on-PD}}(\lambda, \theta) d\lambda d\theta} \quad (3)$$

is the efficiency, relative to  $\eta_{\text{CCE}}$ , at which the PD converts to photocurrent the photons reaching it from the LED. That is,  $\eta_{\text{matching}}$  is the spectral matching efficiency of the PD.

### 6. Optics simulations

The details of the internal optical coupling in the DDS, in terms of  $\chi_{\text{optical}}(\lambda, \theta)$ , that is, how well light reaches the PD from the LED, are not readily measurable. From optics simulations, with the thickness of the varying layers in the DDS, together with the refractive indexes of the constituent materials of each layer [39–47], we can, however, obtain the reflection, transmission, and absorption in the varying layers as a function of wavelength, propagation angle, and polarization state. For these simulations, we use a one-dimensional version of the Fourier modal method (FMM) [48], which thus gives equivalent results as the one-dimensional rigorous coupled-wave analysis (RCWA) or the transfer matrix method (TMM) (see Sec. S6.1 within the Supplemental Material [49] for details of the FMM simulations).

To allow an easy-to-apply analysis, we develop for this study an approximate, iterative method to model the emission from the LED in the optical DDS stack, that is, to calculate  $\chi_{\text{optical}}(\lambda, \theta)$  and  $\Phi_{\text{LED-on-PD}}(\lambda, \theta)$  (see Sec. S6.2 within the Supplemental Material [50] for details). We divide the DDS into two subsystems, one above the LED and one below the LED. We include with the above FMM the interference effects of the emitted light through the layers of each subsystem, with a noncoherent coupling between the top and the bottom side. This approximate

coupling is motivated by the fact that the backreflection from the PD toward the LED tends to be weak. In contrast, this approach is not applicable, for example, for a case where the DDS consists of a resonant cavity with an additional mirror placed below the PD—there, optical cavity modes would set up inside the DDS due to the interference effects through the whole DDS, and a more tedious, coherent optics simulation, e.g., Refs. [38,51], of the full DDS stack is required.

## III. RESULTS AND DATA ANALYSIS

### A. Electrical measurements: $I$ - $V$ data

The results from the  $I$ - $V$  measurements are shown in Fig. 2(a) as a function of the external voltage on the LED and in Fig. 2(b) as a function of LED internal bias as explained below. Figure 2(c) shows the corresponding CQE, which reaches a peak value of approximately equal to 70%, similar as in Ref. [26], where the drop from a value of 1 is largely accredited to optical losses within the DDS. In Ref. [26], it was indicated that the CQE is mostly limited by optical photodetection losses, which we investigate in more detail below.

While the maximum applied bias  $U_1$ , as seen in Fig. 2(a), exceeds 3 V, the internal bias  $U$  across the LED does not exceed the GaAs band-gap bias (1.42 V), when taking into account the voltage drop across the measurement setup's external resistance, which is on the order of several ohms. Figure 2(b) shows the same  $I$ - $V$  curve but now as a function of  $U$ , with  $U$  extracted from the PD current  $I_2$  by considering that it is directly (linearly) proportional to the radiative recombination current of the LED, and thus can be expressed as  $I_2 = I_\alpha \times \exp(qU/kT)$ . Here,  $I_\alpha$  is assumed to be a constant prefactor. At low enough applied biases, the voltage drop due to external resistance is negligible and  $U \approx U_1$ , from which  $I_2$  as a function of  $U_1$  can be used to estimate  $I_\alpha$ . This  $I_\alpha$  can in turn be used to establish a correspondence between  $I_2$ ,  $U$ , and  $U_1$  (see Ref. [26] for more details on this method).

It is worth noticing that the CQE of HJ-1, the MBE grown sample, seems to be much lower at low currents, but rises steeply at high currents to even overtake the CQE of HJ-2 and DHJ-1, which are grown using MOVPE [see Fig. 2(c)]—the maximum CQE value is  $\eta_{\text{CQE}} = 0.707$ , 0.655, and 0.686 for HJ-1, HJ-2, and DHJ-1, respectively. Such CQE behavior with increasing current indicates differences in the MBE and MOVPE grown structures since HJ-1 and HJ-2 have nearly identical structure, other than the presence of the ODR in HJ-1. It is likely that HJ-1 has a higher defect density or more intrinsic active region, possibly originating from differing growth technique as well as conditions in every individual reactor rather than the exact type of reactor. Higher defect density could result in high

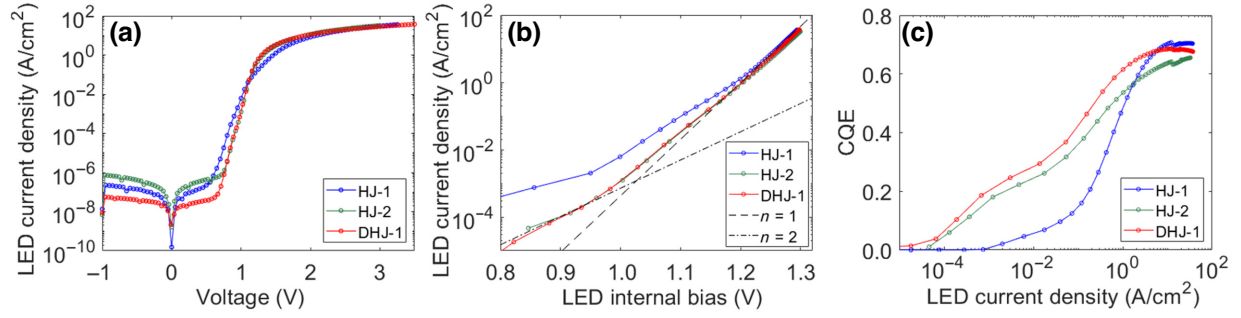


FIG. 2. (a)  $J$ - $V$  curves for the LED ( $J_2$ ) as a function of applied LED bias ( $U_1$ ) with the PD in short circuit ( $U_2 = 0$ ). (b) As (a) but plotted with respect to LED internal bias ( $U$ ) with ideality factors  $n = 1$  and  $n = 2$  added as guidelines. (c) CQE ( $\eta_{\text{CQE}}$ ) as a function of LED current density.

losses at low currents, but the defect recombination centers could fill up at high current level, thus saturating the losses.

### B. Optical measurements: PD EQE, PD $R$ , PD IQE, PD CCE, and LED EL

Figure 3(a) shows the measured EQE,  $\eta_{\text{PD}}^{\text{EQE}}(\lambda)$ , as well as the reflectance  $R$  of the PD-only devices together with  $\Phi_{\text{EL}}(\lambda)$ , the EL spectrum of the LED. To assess the efficiency of the PD for the DDS configuration where the external reflection does not show up, we correct for the reflection loss in the EQE measurements. Therefore, Fig. 3(b) shows the reflectance-corrected EQE,  $\eta_{\text{PD}}(\lambda) = (\eta_{\text{PD}}^{\text{EQE}}(\lambda))/(1 - R(\lambda))$ , which coincides with the definition of the (wavelength-dependent) IQE of a conventional (non-DDS) PD. From Fig. 3(b), we estimate the maximum value for the PD IQE for HJ-1, HJ-2, and DHJ-1 to  $\eta_{\text{PD-max}} = 86\%$ ,  $84\%$ , and  $93\%$ , respectively.

Furthermore, we see from Fig. 3(b) that  $\eta_{\text{PD}}(\lambda)$  drops rapidly at  $\lambda \approx 870$  nm, while the EL spectrum peaks there, as expected due to the room-temperature band gap of approximately 1.42 eV of GaAs [33], which corresponds to a wavelength of approximately 870 nm. Due to the use of the same band-gap material for the LED and PD, the long-wavelength tail of  $\Phi_{\text{EL}}(\lambda)$  extends into the region where  $\eta_{\text{PD}}(\lambda)$  drops rapidly. It clearly leads to the issue of imperfect absorption of the LED light by the PD. Such spectral mismatch should show up as a drop in  $\eta_{\text{matching}}$ —this fact is analyzed in more detail below in Sec. III D.

In Fig. 3(a), we see a difference in the measured reflectance between HJ-2 and DHJ-1, despite them having a very similar structure [which also results in a very similar modeled reflectance as seen in Fig. S7(b) within the Supplemental Material [52]]. HJ-2 shows a clearly lower measured reflectance than DHJ-1. This can be explained by the fact that the HJ-2 PD-only sample has been used for another experiment where an Al layer was deposited on the surface and later etched away, resulting in increased surface roughness. In order to assess whether this reduction in

reflectance is a scattering effect or an antireflection effect, we measure the reflectance spectra with the integrating sphere (see Fig. S4 within the Supplemental Material [53] for the spectra), which confirms the measured reflectance with the FilmTek setup of all samples within the accuracy of  $\pm 1\%$  (absolute) of the integrating sphere measurements. Hence, the induced surface roughness on the HJ-2 PD-only sample only gives rise to an antireflection effect, and the reflectance measured by the FilmTek setup can be used for correcting the EQE spectra, as performed for Fig. 3(b).

To estimate the CCE, we simulate the absorption of externally incident light in the active region of the PD and compare it to the measured EQE. This analysis indicates a CCE of  $\eta_{\text{CCE}} = 90\%$ ,  $88\%$ , and  $95\%$  for HJ-1, HJ-2, and DHJ-1, respectively (see Sec. S7 within the Supplemental Material for details). We use these values for  $\eta_{\text{CCE}}$  in Eqs. (1) and (3) in the below analysis.

### C. Coupling from LED toward PD

Above, we obtain  $\eta_{\text{PD}}(\lambda)$ ,  $\eta_{\text{CCE}}$ , and  $\Phi_{\text{EL}}(\lambda)$ . However, for analysis of the coupling of radiation from the LED to the PD, in terms of the photodetection efficiency  $\xi$  in Eq. (1), we need knowledge also of  $\chi_{\text{optical}}(\lambda, \theta)$ , the coupling of light from the LED to the PD inside the DDS, for which we use modeling.

More specifically, for the calculation of both  $\eta_{\text{optical}}$  and  $\eta_{\text{matching}}$  in Eqs. (2) and (3), we need knowledge of  $\Phi_{\text{LED-on-PD}}(\lambda, \theta) = \chi_{\text{optical}}(\lambda, \theta)\Phi_{\text{LED}}(\lambda, \theta)$ . For this analysis, we assume isotropic emission for the internal EL, which results in an angle dependence given by  $\sin(\theta)\cos(\theta)$  [55] [the  $\cos(\theta)$  term originates from the projection of the intensity flowing through the transverse plane of the DDS and the  $\sin(\theta)$  term from the solid-angle dependence]. Furthermore, we assume that the inherent emission in the LED is not polarization dependent. We approximate the inherent emission of the LED by the externally measured EL spectrum  $\Phi_{\text{EL}}(\lambda)$ . Thus, we use below  $\Phi_{\text{LED}}(\lambda, \theta) = \Phi_{\text{EL}}(\lambda)\sin(\theta)\cos(\theta)$  to estimate the emission into a direction forming an angle  $\theta$  with direct

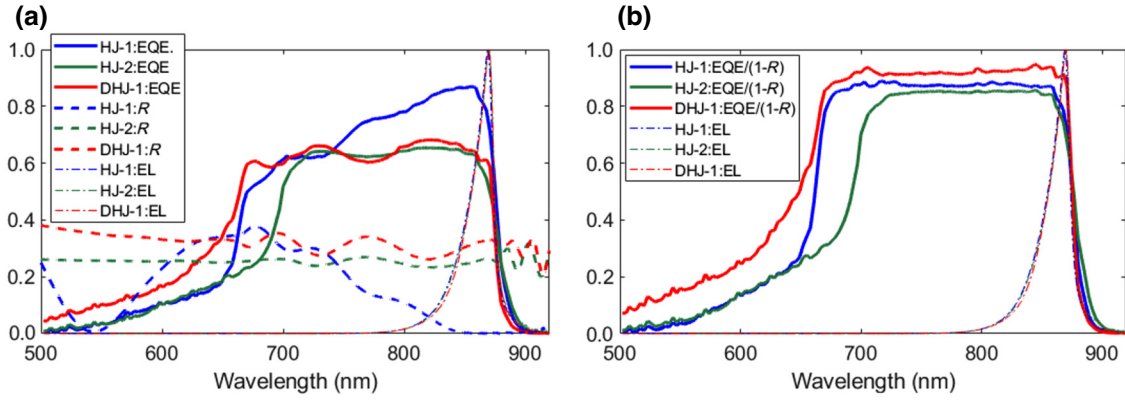


FIG. 3. (a) Measured EQE ( $\eta_{\text{PD}}^{\text{EQE}}$ ),  $R$ , and (normalized) EL spectra ( $\Phi_{\text{EL}}$ ). (b)  $\eta_{\text{PD}}(\lambda) = (\eta_{\text{PD}}^{\text{EQE}}(\lambda))/(1 - R(\lambda))$  shown together with EL.

incidence. We use optics simulations with FMM for calculating  $\chi_{\text{optical}}(\lambda, \theta)$  and  $\Phi_{\text{LED-on-PD}}(\lambda, \theta)$ , including their dependence on the polarization state (see Sec. II B 6 above).

The resulting coupling from the LED to the PD,  $\eta_{\text{optical}}$  in Eq. (2), and the accompanying absorption losses are summarized in Table II for the three DDSs. The samples without ODRs, that is, HJ-2 and DHJ-1, show  $\eta_{\text{optical}} \approx 91\%$ , mainly limited by absorption of 8% in the top mirror. By moving to the ODR design in HJ-1, with 93% of the top surface covered by the ODR and remaining 7% by similar GaAs top contact as in HJ-2 and DHJ-1,  $\eta_{\text{optical}}$  increases to approximately equal to 96%, mainly thanks to a decrease in the absorption in the top mirror, but partly also thanks to a decrease in the absorption in the top GaAs contact layer from approximately equal to 1% to less than 0.1%. Thus, it appears that the optical coupling from the LED to the PD is at a rather high level in the ODR device. We note here that a strong angular dependence is seen in HJ-1 where the loss to the Au mirror drops rapidly for angles beyond  $35^\circ$  (see Figs. S6–S8 within the Supplemental Material [56]), which is the critical angle between the (Ga, In)P layer and the SiN layer in the ODR.

#### D. Spectral matching of PD to LED spectrum

For calculating  $\eta_{\text{matching}}$  in Eq. (3), we use for  $\chi_{\text{PD}}(\lambda, \theta)$  the measured  $\eta_{\text{PD}}(\lambda)$  for each of the three samples (and correct it through modeling for the minor <1% absorption in the middle GaAs contact layer), the  $\eta_{\text{CCE}}$  extracted

from the PD EQE measurements, and  $\Phi_{\text{LED-on-PD}}(\lambda, \theta)$ , the spectrum reaching the PD, which is obtained from the simulations performed in Sec. III C. We obtain for HJ-1, HJ-2, and DHJ-1, respectively,  $\eta_{\text{matching}} = 0.845, 0.824$ , and  $0.861$ . Thus, the HJ and DHJ PDs give rather similar spectral matching to the EL spectrum. This is expected since (1) the EL spectrum, even after the optical losses during coupling to the PD, is centered close to the band-gap wavelength (see Fig. S5 within the Supplemental Material [57]), (2) the DHJ PD shows a more boxlike EQE, with high values almost directly below the band-gap wavelength and low values almost directly above the band-gap wavelength, while (3) the HJ PDs, on the other hand, show a smoother transition around the band-gap wavelength, losing some of the shorter wavelength photons in detection, but gaining some longer wavelength photons in compensation.

#### 1. Power dependence of PD EQE

The above PD EQE measurements with QEX7 are performed at low excitation power (approximately equal to  $0.3 \mu\text{W}$ ) resulting in low photocurrents (approximately equal to  $0.1 \mu\text{A}$ ). However, as seen in Fig. 2(b), the CQE of our device peaks at much higher currents (approximately equal to 80–240 mA depending on the device). Therefore, we address the power dependence of the PD EQE using a home-made setup based on a supercontinuum laser allowing higher powers to be reached (Fig. 4); see Ref. [35] for technical details of these EQE measurements.

TABLE II. Simulated efficiency at which light reaches from the LED to the PD for HJ-1, HJ-2, and DHJ-1 together with the three absorption losses present.

	$\eta_{\text{optical}}$	Absorption in AuZn mirror	Absorption in top $p$ GaAs	Absorption in middle $n$ GaAs
HJ-1 (with ODR)	0.963	0.030	0.001	0.007
HJ-2 (no ODR)	0.909	0.079	0.011	0.006
DHJ (no ODR)	0.910	0.079	0.011	0.006



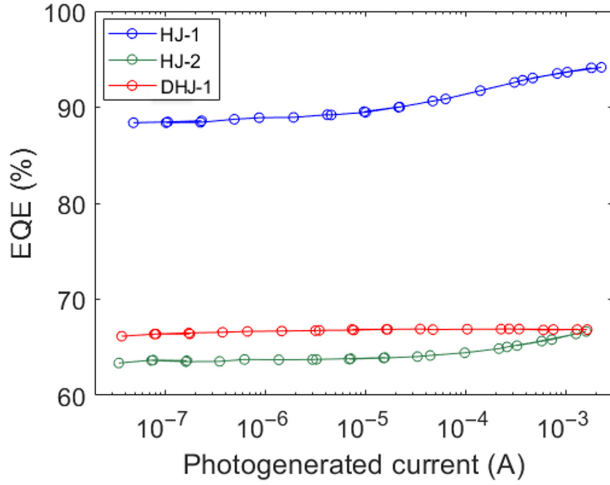


FIG. 4. EQE dependence on the current photogenerated by the PD with varied power of the incident light at 844.5-nm wavelength, which is the longest wavelength accessible in the home-built supercontinuum-laser-based EQE setup and close to the EL emission peak wavelength at approximately 870 nm. Note that the CQE peak in Fig. 2(c) occurs at a current of approximately equal to 80–240 mA depending on device, while the EQE characterization in Figs. 2(a) and 2(b) is performed at a current of approximately equal to 0.1  $\mu$ A.

In Fig. 4, HJ-1 and HJ-2 show an increase by approximately 7% (rel.) in PD EQE with increasing power of the incident light, while DHJ-1 does not show any significant change over the measured nearly 5 orders of magnitude in power increase. Note that the power dependence is shown for up to 2 mA in photocurrent, limited by the available laser power, which is still some 40–120 times lower than the peak CQE current. However, HJ-1 shows a tendency toward saturation in EQE already at that 2 mA in Fig. 4, which makes us believe that the 7% (rel.) EQE increase for the HJ PDs is a good approximation for the value at the CQE peak. Thus, we expect  $\eta_{\text{PD-max}}$  of HJ-1 and HJ-2 to increase by 7% (rel.) compared to the values extracted above with QEX-7. The above 7% relative increase for HJ-1 and HJ-2 brings their  $\eta_{\text{PD-max}}$  to 0.92 and 0.90, respectively, comparable to the power independent  $\eta_{\text{PD-max}}$  of 0.93 for the DHJ PD.

We expect that the optical properties of the materials in the PDs are rather independent of the illumination intensity

over the range considered in Fig. 4. Therefore, we assign the increase in  $\eta_{\text{PD-max}}$  of HJ-1 and HJ-2 to an increase in their CCE. We might be observing saturation of interface recombination around the active region in the HJ PDs with increasing power of the incident light, that is, increasing photogeneration rate [58]. With the above 7% (rel.) increase for HJ-1 and HJ-2 assigned to the CCE, we end up with  $\eta_{\text{CCE}} = 96\%$ ,  $94\%$ , and  $95\%$  for HJ-1, HJ-2, and DHJ-1, respectively.

#### IV. DISCUSSION OF OPTICAL COUPLING AND ITS EFFECT TOWARD ACHIEVING ELC

The main extracted values are summarized in Table III. For the IQE of the LED, we obtain for the three samples values in the range of 0.90–0.93. The lower value for the MBE-grown sample corresponds well with the observations made in Fig. 2 with possibly higher defect density. However, such an estimate for the LED IQE should be taken with caution due to the multiple steps and approximations, combining varying measurements and modeling, in the analysis. All three devices show  $\text{PCE} > 1$ , indicating that internal cooling of the LED is already present in the devices (see Fig. S8 within the Supplemental Material [59]). In this paper's context, however, the more useful (and reliable) information relates to the coupling of radiation from the LED to the PD, in terms of the photodetection efficiency  $\xi$ , and breaking it down to its constituents  $\eta_{\text{optical}}$ ,  $\eta_{\text{matching}}$ , and  $\eta_{\text{CCE}}$  [see also Eq. (1)].

In this way, we identify three main aspects for improvement in the photodetection efficiency  $\xi$  in the DDS: (1) The ODR structure increases the optical coupling from the LED to the PD, that is,  $\eta_{\text{optical}}$ , by approximately 5% (absolute)—see Table III. However, the current ODR design still leaves space for further 4% (absolute) improvement in  $\eta_{\text{optical}}$ . These losses occur predominantly in the AuZn mirror. Therefore, a more dedicated ODR design could further boost  $\xi$ . (2) We find in  $\eta_{\text{CCE}}$  room for improvement by approximately equal to 5% (absolute), which calls for a more dedicated electrical design of the PD. (3) There is an approximately equal to 14% boost awaiting with optimization of  $\eta_{\text{matching}}$ , which is limited by the transmission loss through the PD in the vicinity of the bandgap of the GaAs active region of the PD.

TABLE III. Summary of the efficiencies for each studied device. The reported  $\eta_{\text{CCE}}$ , and consecutively also the  $\xi = \eta_{\text{optical}}\eta_{\text{matching}}\eta_{\text{CCE}}$ , includes for HJ-1 and HJ-2 the 7% relative increase found in Fig. 4 at high illumination power. The IQE of the LED is extracted as  $\eta_{\text{LED}} = \eta_{\text{CQE}}/\xi$ , and for details of  $\eta_{\text{PCE}}$ , the PCE of the ELC, see Fig. S8 within the Supplemental Material [59]. The confidence in the reported values is the highest in the columns further to the left.

Sample	Peak $\eta_{\text{CQE}}$	$\eta_{\text{CCE}}$	$\eta_{\text{optical}}$	$\eta_{\text{matching}}$	$\xi$	$\eta_{\text{LED}}$	Peak $\eta_{\text{PCE}}$
HJ-1	0.707	0.96	0.962	0.845	0.78	0.90	1.04
HJ-2	0.655	0.94	0.909	0.824	0.70	0.93	1.02
DHJ-1	0.686	0.95	0.910	0.861	0.74	0.93	1.02

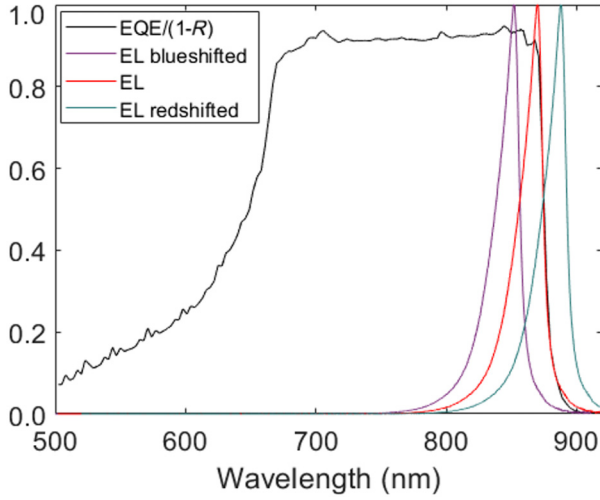


FIG. 5. Shifting of the LED EL spectrum by 30 meV with respect to  $\eta_{\text{PD}}^{\text{EQE}}(\lambda)/(1-R)$  for DHJ-1.

To increase  $\eta_{\text{matching}}$ , the transmission losses in the PD could be decreased either by making a thicker active region layer or by making a thin-film device with the whole DDS within a mirror cavity with a mirror underneath the PD [51]. Alternatively, the transmission loss in the PD can be circumvented if the LED spectrum is blueshifted into the region of high IQE of the PD. Figure 5 illustrates for DHJ-1 DDS the effect of blue- and redshifting the emission spectrum of the LED by just 30 meV (from room-temperature value). With the blueshift,  $\eta_{\text{matching}}$  increases to 0.97 from 0.86, while the redshift causes a drop to 0.39. It is worth noting, that such a blueshift could occur in a device with thermal insulation between the LED and PD if the LED cools down to at least 230 K in operation, in which case the GaAs LED emission blueshifts by 30 meV due to the band-gap decrease in GaAs with decreasing temperature [33].

However, in our current DDS configuration, as well as in devices where cooling is intended for small temperature differences, a shift of LED and/or PD band gap would still be required for the PD to efficiently absorb the light from the LED. Furthermore, if the DDS is, instead of cooling applications, used for waste-heat-recovery applications [60,61], the LED operates at a much higher temperature than the PD, and the temperature difference induces a relative redshift of the LED spectrum. Then, a careful choice of the materials and their band gaps for the LED and PD active regions to efficiently match the LED emission spectrum to the region of high PD EQE would be crucial, as suggested also in Refs. [60,62]. In contrast to the cooling applications where a poor spectral matching will primarily just reduce the coefficient of performance (COP) of the cooling, in the waste-heat energy-harvesting applications a sufficient spectral match is crucial for the energy-harvesting itself.

## V. CONCLUSION

We study the coupling of emitted light from the LED to the PD in the DDS with a combination of measurements and optics simulations. The performance of the PD is assessed by measuring the EQE of dedicated PD-only devices, correcting for measured external reflection losses. Furthermore, we measure the external EL of the LED to approximate the internal emission spectrum. However, the transport of light from the LED to the PD is not readily measurable, and we turn to optics simulations. The simulation of the coupling of internal emission from the active region in the LED toward the PD is performed with an iterative approach, developed for this study.

Our analysis approach allows decomposition of the internal coupling in the DDS to three multiplicative efficiency factors:  $\eta_{\text{optical}}$ ,  $\eta_{\text{matching}}$ , and  $\eta_{\text{CCE}}$ . The analysis revealed that the largest room for improvement, with 14% (absolute), lies in  $\eta_{\text{matching}}$ , which is the efficiency (normalized to  $\eta_{\text{CCE}}$ ) at which the PD manages to take advantage of the spectrum incident on it from the LED. This large drop in efficiency occurs due to the transmission losses through the PD when using a GaAs PD for a GaAs LED. We note that in a DDS device that efficiently cools the LED through ELC, with thermal insulation to the PD, this efficiency ought to increase due to the relative blueshift of the LED emission to the region of high IQE of the PD. Alternatively, we offer as a solution band-gap-tuning by materials choice for the LED and/or PD to give rise to such a relative spectral shift between them. The second largest room for improvement, with 5% (absolute) lies in  $\eta_{\text{CCE}}$ . To boost  $\eta_{\text{CCE}}$ , a careful optimization of the electrical design of the PD is needed. Finally, when an ODR is used at the top side of the LED, there is still 4% (absolute) room for improvement in  $\eta_{\text{optical}}$ , the efficiency at which the emission from the LED reaches the PD. Here, we recommend an even more dedicated ODR design to boost  $\eta_{\text{optical}}$ .

## ACKNOWLEDGEMENTS

The authors acknowledge the provision of facilities and technical support by Aalto University at Micronova Nanofabrication Centre, Professor M. Guina for the MBE samples, and Dr Janne Halme for access and training to the QEX7 setup. This project has received funding from the European Union's Horizon 2020 research and innovation programme under Grants Agreement No. 964698 (OPTAGON) and No. 9519769 (TPX-POWER).

## APPENDIX A: QUANTITIES USED IN THE ANALYSIS

A list of the quantities used in the analysis is given in Table IV.

TABLE IV. Summary of the quantities used in the electro-optical analysis in this paper and how they are extracted.

Quantity	Expression	Extraction	Defined in Sec.
ELC PCE	$\eta_{\text{PCE}} = \frac{\eta_{\text{CQE}}}{\xi} \times \frac{E_{\text{ph}}}{qU} =$ $\eta_{\text{LED}} \times \frac{E_{\text{ph}}}{qU}$	From $\eta_{\text{CQE}}$ , $\xi$ , and $U$	II B 1
Internal voltage bias of LED	$U$	From $I$ - $V$ measurements	II B 1
LED IQE	$\eta_{\text{LED}} = \frac{\eta_{\text{CQE}}}{\xi}$	From $\eta_{\text{CQE}}$ and $\xi$	II B 1
Coupling quantum efficiency	$\eta_{\text{CQE}} = \frac{I_2}{I_1}$	From $I_2$ , measured current from PD, and $I_1$ , measured current to LED	II B 1
Photodetection efficiency in DDS	$\xi = \eta_{\text{optical}} \eta_{\text{matching}} \eta_{\text{CCE}}$	From $\eta_{\text{optical}}$ , $\eta_{\text{matching}}$ , and $\eta_{\text{CCE}}$	II B 5
Efficiency at which photons emitted from the LED reach the PD	$\eta_{\text{optical}}$	From $\Phi_{\text{LED}}$ and $\Phi_{\text{LED-on-PD}}$	II B 5
Spectral matching efficiency of the PD (relative to incident LED light)	$\eta_{\text{matching}}$	From $\chi_{\text{PD}}$ and $\Phi_{\text{LED-on-PD}}$	II B 5
CCE of PD	$\eta_{\text{CCE}}$	From $\eta_{\text{PD}}^{\text{EQE}}(\lambda)$ with optics simulations	II B 5
PD IQE in DDS	$\chi_{\text{PD}}(\lambda, \theta)$	From $\eta_{\text{PD}}$ , with correction from optics simulations for minor, <0.5%, absorption in the middle GaAs layer.	II B 5
Optical coupling from LED to PD in DDS	$\chi_{\text{optical}}(\lambda, \theta)$	From optics simulations	II B 5
Internal EL spectrum of the LED in the DDS	$\Phi_{\text{LED}}(\lambda, \theta)$	Estimated from $\Phi_{\text{EL}}$	II B 5
Spectrum incident on the PD in the DDS	$\Phi_{\text{LED-on-PD}}(\lambda, \theta) =$ $\chi_{\text{optical}}(\lambda, \theta) \Phi_{\text{LED}}(\lambda, \theta)$	From $\chi_{\text{optical}}$ and $\Phi_{\text{LED}}$	II B 5
External EL spectrum of LED	$\Phi_{\text{EL}}(\lambda)$	Measured	II B 2
EQE of PD-only devices	$\eta_{\text{PD}}^{\text{EQE}}(\lambda)$	Measured	II B 3
Reflectance of PD-only devices	$R(\lambda)$	Measured	II B 4
IQE of PD-only devices	$\eta_{\text{PD}}(\lambda) =$ $\eta_{\text{PD}}^{\text{EQE}}(\lambda)/[1 - R(\lambda)]$	From $\eta_{\text{PD}}^{\text{EQE}}$ and $R$	III B

- [1] J. Cho, J. H. Park, J. K. Kim, and E. F. Schubert, White light-emitting diodes: History, progress, and future, *Laser Photonics Rev.* **11**, 1600147 (2017).
- [2] M. Kneissl, T.-Y. Seong, J. Han, and H. Amano, The emergence and prospects of deep-ultraviolet light-emitting diode technologies, *Nat. Photonics* **13**, 233 (2019).
- [3] H. E. Lee, J. H. Shin, J. H. Park, S. K. Hong, S. H. Park, S. H. Lee, J. H. Lee, I.-S. Kang, and K. J. Lee, Micro light-emitting diodes for display and flexible biomedical applications, *Adv. Funct. Mater.* **29**, 1808075 (2019).
- [4] T. Sadi, I. Radevici, and J. Oksanen, Thermophotonic cooling with light-emitting diodes, *Nat. Photonics* **14**, 4 (2020).
- [5] K. Lehovc, C. A. Accardo, and E. Jamgochian, Light emission produced by current injected into a green silicon-carbide crystal, *Phys. Rev.* **89**, 20 (1953).
- [6] J. Tauc, The share of thermal energy taken from the surroundings in the electro-luminescent energy radiated from

a p-n junction, *Czechoslovakij Fiziceskij Zurnal* **7**, 275 (1957).

- [7] R. J. Keyes and T. M. Quist, Recombination radiation emitted by gallium arsenide, *Proc. RIE* **50**, 1822 (1962).
- [8] G. C. Dousmanis, C. W. Mueller, H. Nelson, and K. G. Petzinger, Evidence of refrigerating action by means of photon emission in semiconductor diodes, *Phys. Rev.* **133**, A316 (1964).
- [9] P. Wurfel, The chemical potential of radiation, *J. Phys. C: Solid State Phys.* **15**, 3967 (1982).
- [10] D. V. Seletskiy, S. D. Melgaard, S. Bigotta, A. Di Lieto, M. Tonelli, and M. Sheik-Bahae, Laser cooling of solids to cryogenic temperatures, *Nat. Photonics* **4**, 161 (2010).
- [11] F. Schreck and K. van Druten, Laser cooling for quantum gases, *Nat. Phys.* **17**, 1296 (2021).
- [12] D. V. Seletskiy, R. Epstein, and M. Sheik-Bahae, Laser cooling in solids: Advances and prospects, *Rep. Prog. Phys.* **79**, 096401 (2016).

- [13] A. Fiorino, L. Zhu, D. Thompson, R. Mittapally, P. Reddy, and E. Meyhofer, Nanogap near-field thermophotovoltaics, *Nat. Nanotechnol.* **13**, 806 (2018).
- [14] M. P. Hehlen, J. Meng, A. R. Albrecht, E. R. Lee, A. Gragossian, S. P. Love, C. E. Hamilton, R. I. Epstein, and M. Sheik-Bahae, First demonstration of an all-solid-state optical cryocooler, *Light: Sci. Appl.* **7**, 15 (2018).
- [15] M. P. Nielsen, A. Pusch, M. H. Sazzad, P. M. Pearce, P. J. Reece, and N. J. Ekins-Daukes, Thermoradiative power conversion from HgCdTe photodiodes and their current–voltage characteristics, *ACS Photonics* **9**, 1535 (2022).
- [16] B. Zhao, S. Buddhiraju, P. Santhanam, K. Chen, and S. Fan, Self-sustaining thermophotonic circuits, *Proc. Natl. Acad. Sci.* **116**, 11596 (2019).
- [17] L. Zhu, A. Fiorino, D. Thompson, R. Mittapally, E. Meyhofer, and P. Reddy, Near-field photonic cooling through control of the chemical potential of photons, *Nature* **566**, 239 (2019).
- [18] R. Mittapally, B. Lee, L. Zhu, A. Reihani, J. W. Lim, D. Fan, S. R. Forrest, P. Reddy, and E. Meyhofer, Near-field thermophotovoltaics for efficient heat to electricity conversion at high power density, *Nat. Commun.* **12**, 4364 (2021).
- [19] D. Fan, T. Burger, S. McSherry, B. Lee, A. Lenert, and S. R. Forrest, Near-perfect photon utilization in an air-bridge thermophotovoltaic cell, *Nature* **586**, 237 (2020).
- [20] J. Song, J. Jang, M. Lim, M. Choi, J. Lee, and B. J. Lee, Thermophotovoltaic energy conversion in far-to-near-field transition regime, *ACS Photonics* **9**, 1748 (2022).
- [21] A. Kohiyama, M. Shimizu, K. Konno, T. Furuhashi, and H. Yugami, Effective photon recycling in solar thermophotovoltaics using a confined cuboid emitter, *Opt. Express* **28**, 38567 (2020).
- [22] C. Lucchesi, D. Cakiroglu, J.-P. Perez, T. Taliercio, E. Tournié, P.-O. Chapuis, and R. Vaillon, Near-field thermophotovoltaic conversion with high electrical power density and cell efficiency above 14%, *Nano Lett.* **21**, 4524 (2021).
- [23] J. Mao, G. Chen, and Z. Ren, Thermoelectric cooling materials, *Nat. Mater.* **20**, 454 (2021).
- [24] P. Santhanam, D. J. Gray, and R. J. Ram, Thermoelectrically Pumped Light-Emitting Diodes Operating above Unity Efficiency, *Phys. Rev. Lett.* **108**, 097403 (2012).
- [25] J. Xue, Y. Zhao, S.-H. Oh, W. F. Herrington, J. S. Speck, S. P. DenBaars, S. Nakamura, and R. J. Ram, Thermally enhanced blue light-emitting diode, *Appl. Phys. Lett.* **107**, 121109 (2015).
- [26] I. Radevici, J. Tiira, T. Sadi, S. Ranta, A. Tukiainen, M. Guina, and J. Oksanen, Thermophotonic cooling in GaAs based light emitters, *Appl. Phys. Lett.* **114**, 051101 (2019).
- [27] S. Fafard and D. P. Masson, 74.7% efficient GaAs-based laser power converters at 808 nm at 150 K, *Photonics* **9**, 8 (2022).
- [28] H. Helmers, E. Lopez, O. Höhn, D. Lackner, J. Schön, M. Schauerte, M. Schachtner, F. Dimroth, and A. W. Bett, 68.9% efficient GaAs-based photonic power conversion enabled by photon recycling and optical resonance, *Phys. Status Solidi RRL – Rapid Res. Lett.* **15**, 2100113 (2021).
- [29] See Supplemental Material at <http://link.aps.org/supplemental/10.1103/PhysRevApplied.19.064054> for a list of all the device layers.
- [30] See Supplemental Material at <http://link.aps.org/supplemental/10.1103/PhysRevApplied.19.064054> for growth details for the MOVPE samples.
- [31] P. Kivisaari, M. Partanen, T. Sadi, and J. Oksanen, Interplay of Photons and Charge Carriers in Thin-Film Devices, *Phys. Rev. Appl.* **16**, 024036 (2021).
- [32] W. A. Callahan, D. Feng, Z. M. Zhang, E. S. Toberer, A. J. Ferguson, and E. J. Tervo, Coupled Charge and Radiation Transport Processes in Thermophotovoltaic and Thermoradiative Cells, *Phys. Rev. Appl.* **15**, 054035 (2021).
- [33] I. Vurgaftman, J. R. Meyer, and L. R. Ram-Mohan, Band parameters for III–V compound semiconductors and their alloys, *J. Appl. Phys.* **89**, 5815 (2001).
- [34] See Supplemental Material at <http://link.aps.org/supplemental/10.1103/PhysRevApplied.19.064054> for measured and modeled EL spectra.
- [35] See Supplemental Material at <http://link.aps.org/supplemental/10.1103/PhysRevApplied.19.064054> for additional technical details of the EQE measurements.
- [36] N. Anttu, V. Dagytė, X. Zeng, G. Otnes, and M. Borgström, Absorption and transmission of light in III–V nanowire arrays for tandem solar cell applications, *Nanotechnology* **28**, 205203 (2017).
- [37] See Supplemental Material at <http://link.aps.org/supplemental/10.1103/PhysRevApplied.19.064054> for details of the total reflectance measurements in an integrating sphere.
- [38] N. Anttu, H. Mäntynen, A. Sorokina, J. Turunen, T. Sadi, and H. Lipsanen, Applied electromagnetic optics simulations for nanophotonics, *J. Appl. Phys.* **129**, 131102 (2021).
- [39] M. D. Sturge, Optical absorption of gallium arsenide between 0.6 and 2.75 eV, *Phys. Rev.* **127**, 768 (1962).
- [40] E. D. Palik, in *Handbook of Optical Constants of Solids*, edited by E. D. Palik (Academic Press, Boston, 1985), pp. 429–443.
- [41] H. C. Casey, D. D. Sell, and K. W. Wecht, Concentration dependence of the absorption coefficient for n– and p–type GaAs between 1.3 and 1.6 eV, *J. Appl. Phys.* **46**, 250 (1975).
- [42] O. J. Glembocki and K. Takarabe, in *Handbook of Optical Constants of Solids*, edited by E. D. Palik (Academic Press, Burlington, 1997), pp. 513–558.
- [43] A. D. Rakić and M. L. Majewski, Modeling the optical dielectric function of GaAs and AlAs: Extension of Adachi’s model, *J. Appl. Phys.* **80**, 5909 (1996).
- [44] S. Adachi, H. Kato, A. Moki, and K. Ohtsuka, Refractive index of  $(\text{Al}_x\text{Ga}_{1-x})_{0.5}\text{In}_{0.5}\text{P}$  quaternary alloys, *J. Appl. Phys.* **75**, 478 (1994).
- [45] D. W. Lynch and W. R. Hunter, in *Handbook of Optical Constants of Solids*, edited by E. D. Palik (Academic Press, Burlington, 1997), pp. 275–367.
- [46] W. S. M. Werner, K. Glantschnig, and C. Ambrosch-Draxl, Optical constants and inelastic electron-scattering data for 17 elemental metals, *J. Phys. Chem. Ref. Data* **38**, 1013 (2009).
- [47] J. Kischkat, S. Peters, B. Gruska, M. Semtsiv, M. Chashnikova, M. Klinkmüller, O. Fedosenko, S. Machulik, A.



- Aleksandrova, G. Monastyrskiy, Y. Flores, W. T. Masselink, Mid-infrared optical properties of thin films of aluminum oxide, titanium dioxide, silicon dioxide, aluminum nitride, and silicon nitride, *Appl. Opt.* **51**, 6789 (2012).
- [48] N. Anttu and H. Q. Xu, Scattering matrix method for optical excitation of surface plasmons in metal films with periodic arrays of subwavelength holes, *Phys. Rev. B* **83**, 165431 (2011).
- [49] See Supplemental Material at <http://link.aps.org/supplemental/10.1103/PhysRevApplied.19.064054> for details of the FMM simulations.
- [50] See Supplemental Material at <http://link.aps.org/supplemental/10.1103/PhysRevApplied.19.064054> for additional details of the iterative method to model the emission from the LED in the optical DDS stack.
- [51] P. Kivisaari and J. Oksanen, Resonance effects in the radiation transfer of thin-film intracavity devices, *Appl. Phys. Lett.* **121**, 191101 (2022).
- [52] See Supplemental Material at <http://link.aps.org/supplemental/10.1103/PhysRevApplied.19.064054> for modeled reflectance spectra.
- [53] See Supplemental Material at <http://link.aps.org/supplemental/10.1103/PhysRevApplied.19.064054> for reflectance spectra measured with the integrating sphere.
- [54] See Supplemental Material at <http://link.aps.org/supplemental/10.1103/PhysRevApplied.19.064054> for technical details for the extraction of CCE.
- [55] N. Anttu, Shockley–Queisser detailed balance efficiency limit for nanowire solar cells, *ACS Photonics* **2**, 446 (2015).
- [56] See Supplemental Material at <http://link.aps.org/supplemental/10.1103/PhysRevApplied.19.064054> for modelled optical spectra.
- [57] See Supplemental Material at <http://link.aps.org/supplemental/10.1103/PhysRevApplied.19.064054> for measured and modelled EL Spectra.
- [58] N. P. Wells, T. U. Driskell, A. I. Hudson, S. D. LaLumondiere, W. T. Lotshaw, D. V. Forbes, and S. M. Hubbard, Carrier quenching in InGaP/GaAs double heterostructures, *J. Appl. Phys.* **118**, 065703 (2015).
- [59] See Supplemental Material at <http://link.aps.org/supplemental/10.1103/PhysRevApplied.19.064054> for additional details for the PCE of the ELC.
- [60] B. Zhao, P. Santhanam, K. Chen, S. Buddhiraju, and S. Fan, Near-field thermophotonic systems for low-grade waste-heat recovery, *Nano Lett.* **18**, 5224 (2018).
- [61] T. Sadi, I. Radevici, B. Behaghel, and J. Oksanen, Prospects and requirements for thermophotonic waste heat energy harvesting, *Sol. Energy Mater. Sol. Cells* **239**, 111635 (2022).
- [62] J. Legendre and P.-O. Chapuis, GaAs-based near-field thermophotonic devices: Approaching the idealized case with one-dimensional pn junctions, *Sol. Energy Mater. Sol. Cells* **238**, 111594 (2022).